Eur. J. Mech., B/Fluids, **12**, n° 1, 107-134, 1993

2-D wavelet transforms: generalisation of the Hardy space and application to experimental studies

T. DALLARD and G. R. SPEDDING *

ABSTRACT. – The wavelet transform has recently been extensively used and discussed as a tool for signal analysis and as a function basis. Most applications have thus far concerned 1-D signals. Here, the wavelet definition is generalised in $L(R^2)$ function space, and its application to two-dimensional signals is discussed. The different possible wavelet functions to do this are examined. In general, they may be either *real* or *complex*, but the latter are preferred since both phase and amplitude components of the complex transform convey useful information. The new 2-D wavelet functions *Halo* and *Arc* are introduced, together with the straightforward extension to 2-D of the complex Morlet wavelet, and their behaviour is examined analytically, and on selected test signals.

The properties of *directional* wavelet functions are compared with those of *cylindrical* ones. The first are more precise in wavenumber space, but require initial information concerning the input signal. In the absence of this information, interpretation of the phase is difficult and error-prone. By contrast, the second type of wavelet is simple to use on data where the direction of the wavenumber vector is known only imprecisely in advance, or where it may take on different orientations in different spatial locations. This information may then be used in a second pass, where the transform is with a directional-specific wavelet function.

The implications of these results for the successful application of 2-D wavelet transforms to experimental fluid mechanics data is discussed. A specific application to fluid turbulence is described where, it is shown that, in an acoustically-forced mixing layer, phase defects are the sites of local scale transitions. This can be modified by changing the pattern of forcing. These conclusions, requiring the *local* scale decomposition and phase information around the defects, would have been hard, if not impossible, to come by in any other way.

1. Introduction

The *wavelet transform* has been successfully used in the analysis of signals in divers fields such as telecommunications [Meyer, 1990], and machine vision [Mallat, 1989 *a*]. It has the advantage over conventional Fourier analysis in that information is localised in both physical and wavenumber space. The idea of localising the information from the Fourier transform in physical space dates back to the early work of Gabor [1945], where the basis function is localised inside a gaussian envelope. Inspired by the apparent existence of such a decomposition in early retinal information processing in higher vertebrates, Gabor functions form the basis of much work in pattern recognition research [Daugman, 1988]. This *windowed* Fourier transform has a constant window width,

* Department of Aerospace Engineering, University of southern California, Los Angeles, CA 90089-1191, U.S.A.

EUROPEAN JOURNAL OF MECHANICS, B/FLUIDS, VOL. 12, N° 1 1993
0997-7546/93/01 107 28/$ 4.80/

regardless of the wavenumber, and so has largely been supplanted by the wavelet transform, developed by Grossman & Morlet [1984]. One single parameter, a, determines the wavenumber, and a second parameter, b, specifies the spatial location. A common analogy is made between these two parameters and the optics and stage motion, respectively, of a microscope. Morlet has also observed how the wavelet transform presents information similar to the musician's stave, which specifies both the frequency of the note, and the time at which it is played.

These properties have been exploited in many fields: pioneering examples in mathematics [Meyer, 1987; Jaffard & Meyer, 1987], electrocardiography [Tuteur, 1987], geophysics [Larsonneur & Morlet, 1987], fluid mechanics [Liandrat & Moret-Bailly, 1990], and fractal analysis [Arneodo *et al.* 1988, Argoul *et al.* 1988, 1990] are all testimony to the broad potential of this technique. A mathematical introduction has recently appeared by Daubechies [1992], and Farge [1992] has provided a most useful review of the application of the wavelet decomposition to turbulence in fluids.

With some notable exceptions, most of the examples and applications have thus far been restricted to 1-D signals (consult [Grossmann *et al.*, 1987] for an overview). Applications of 2-D transforms to psycho-physiology, computer vision and image processing have been discussed by Mallat [1989 *a*, *b*], and the extension of the Morlet wavelet to two dimensions and its application to 2-D fluid turbulence data has been discussed by Farge *et al.* [1989]. Murenzi [1987, 1989] has considered the mathematical generalisation of the 1-D transform to the n-D case, and Antoine *et al.* [1992] have recently compared properties of existing 2-D wavelets. This paper presents in some detail the extension of the wavelet transform techniques to 2-D, including some of the existing work together with a new wavelet function, which is shown to have comparatively favourable properties when applied to certain classes of 2-D signals.

2. The wavelet basis

Mathematically, the wavelet transform is equivalent to using a family of functions other than the usual:

$$(g_{\mathbf{k}})_{\mathbf{k}\in\mathbf{R}^2}:\mathbf{r}\to\exp(i\mathbf{k}.\mathbf{r}) \quad \text{on } \mathrm{L}(\mathbf{R}^2)$$
$$(\text{or } (g_{\omega})_{\omega\in\mathbf{R}}:x\to\exp(i\omega.x) \text{ on } \mathrm{L}(\mathbf{R}^1))$$

as a projection basis for the function on $\mathrm{L}(\mathbf{R}^2)$ (or $\mathrm{L}(\mathbf{R}^1)$). The new family is generated by a *wavelet* function $g(\mathbf{r})$:

$$(g_{a,\mathbf{b}})_{(a,\mathbf{b})\in\mathbf{R}^{+*}\times\mathbf{R}^2}:\mathbf{r}\to\frac{1}{a^2}\cdot g\left(\frac{\mathbf{r}-\mathbf{b}}{a}\right) \tag{1}$$

It will also be convenient on occasion to define

$$(g_{a,\mathbf{b}})_{(a,\mathbf{b})\in\mathbf{R}^{+*}\times\mathbf{R}^2}:\mathbf{r}\to\frac{1}{a}\cdot g\left(\frac{\mathbf{r}-\mathbf{b}}{a}\right), \tag{2}$$

so that

$$\iint |g_{a,\mathbf{b}}|^2(\mathbf{r})\,d\mathbf{r} = \iint |g|^2(\mathbf{r})\,d\mathbf{r},$$

rather than

$$\iint |g_{a,\mathbf{b}}|(\mathbf{r})\,d\mathbf{r} = \iint |g|(\mathbf{r})\,d\mathbf{r}.$$

The following analysis deals only with continuous wavelet functions (a and $\mathbf{b}$ vary continuously on $R^{+*} \times R^2$), and without regard to orthogonality. Daubechies [1988] and Meyer [1987] have analysed the discrete wavelet and orthogonal basis functions in some detail.

3. Two-dimensional wavelet transform

Notation

- $L(R^2)$: space of measurable and square integrable 2-D complex functions $f(x, y)$.
- $\mathcal{F}f(\mathbf{k}) = \hat{f}(\mathbf{k}) = \dfrac{1}{2\pi}\iint f(\mathbf{r})\,e^{-i\mathbf{k}\cdot\mathbf{r}}\,d\mathbf{r}$: Fourier transform of f.
- f^*: the complex conjugate of f.
- $\mathcal{W}f = f_W$: wavelet transform of the function f.

3.1. Generalizations of the 1-D transform

The wavelet transform of the function $f(\mathbf{r})$ in $(a, \mathbf{b})$ is the inner product of f with $g_{a,\mathbf{b}}$:

$$f_W(a, \mathbf{b}) = \iint f(\mathbf{r}) \cdot g^*_{a,\mathbf{b}}(\mathbf{r})\,d\mathbf{r} = \frac{1}{a^2} \cdot \iint f(\mathbf{r}) \cdot g^*\left(\frac{\mathbf{r}-\mathbf{b}}{a}\right) d\mathbf{r}. \tag{3}$$

From Parseval's theorem, this may be written as:

$$f_W(a, \vec{\mathbf{b}}) = \iint \hat{f}(\mathbf{k}) \cdot \hat{g}^*(a\mathbf{k})\,e^{i\mathbf{k}.\mathbf{b}}\,d\mathbf{k}. \tag{4}$$

This provides a simple algorithm to compute the wavelet transform, based on the Fourier transform in (4), since it is much simpler to perform a multiplication in Fourier space, rather than a convolution in physical space.

3.2. The notion of Hardy space

For the 1-D wavelet, G & M [1984] introduced the notion of the Hardy function, where, for every *real* signal $s(t)$, a unique *complex* function $S(t)$ is defined so that:

- $\hat{S}(\omega) = 0$ for $\omega \leqq 0$ (definition of a Hardy function)
- $s(t) = \Re[S(t)]$

$\mathscr{H}^1$ is termed the Hardy space, and g is chosen in $\mathscr{H}^1$. S can be defined with the Hilbert operator:

$$\mathrm{H}^1 : s \to (i\mathscr{F}^{-1}\varepsilon\mathscr{F})s \tag{5}$$

with $\varepsilon f(\omega) = (\mathrm{sgn}(\omega))\, f(\omega)$, and so,

$$\mathrm{S} = s - i\mathrm{H}^1 s. \tag{6}$$

From Parseval's Theorem, it is easy to show that:

$$\mathscr{W}^1 s = \frac{1}{2}\mathscr{W}^1 \mathrm{S}. \tag{7}$$

The interest of this formalism is to define for s, a phase and an amplitude, *i.e.* the argument and the modulus of S. As g belongs to $\mathscr{H}^1$, g is complex, and so $\mathscr{W}^1 s$.

So, the phase and the amplitude are both defined for $\mathscr{W}^1 s$ directly connected to s through the restriction of $\mathscr{W}^1$ on $\mathscr{H}^1$. But there is no obvious solution to generalize in a unique way the space $\mathscr{H}^1$ and the operator H^1 in $\mathrm{L}(\mathrm{R}^2)$. The requirement is to redefine the operator ε to bisect R^2 into two parts, π^1 and π^2, such that if $\mathbf{k} \in \pi^1$ then $-\mathbf{k} \in \pi^2$, and,

$$\begin{aligned} \varepsilon f(\mathbf{k}) &= f(\mathbf{k}) \quad \text{if} \quad \mathbf{k} \in \pi^1, \\ \varepsilon f(\mathbf{k}) &= -f(\mathbf{k}) \quad \text{if} \quad \mathbf{k} \in \pi^2. \end{aligned} \tag{8}$$

Now the 1-D formalism may be applied to the 2-D situation with the same results (cf. (5), (6), (7)):

$$\mathrm{S} \in \mathscr{H}^2 \Leftrightarrow \hat{\mathrm{S}}(\mathbf{k}) = 0 \quad \text{for } \mathbf{k} \in \pi^2 \tag{9}$$

$$\mathrm{H}^2 = i\mathscr{F}^{-1}\varepsilon\mathscr{F}$$

$$\mathrm{F}(\mathbf{r}) = f(\mathbf{r}) - i\mathrm{H}^2 f(\mathbf{r}) \quad \text{so } \mathrm{F} \in \mathscr{H}^2 \quad \text{and} \quad \mathscr{W}^2 f = \frac{1}{2}\mathscr{W}^2 \mathrm{F}$$

It remains to define π^1 and π^2. For a *directional* wavelet, the definition is obvious: if $\mathbf{k}_0$ is the direction of the wavelet, then

$$\begin{cases} \mathbf{k} \in \pi^1 \Leftrightarrow \mathbf{k}.\mathbf{k}_0 > 0 \quad \text{or } (\widehat{\mathbf{k}, \mathbf{k}_0}) = \dfrac{\pi}{2} \\ \mathbf{k} \in \pi^2 \Leftrightarrow \mathbf{k}.\mathbf{k}_0 < 0 \quad \text{or } (\widehat{\mathbf{k}, \mathbf{k}_0}) = -\dfrac{\pi}{2} \end{cases}$$

However, if we choose a *cylindrical* wavelet, it is no longer obvious how to define π^1 and π^2. Strictly speaking, the best choice will depend on the signal to be studied, and in most practical applications, the functions are not cylindrical: $f(r)$. So instead, π^1 and π^2

may be defined as two half-planes, with the border (which includes (0, 0)) in the direction where the Fourier transform of the signal has the smallest values (*Fig.* 1 *a*, *b*).

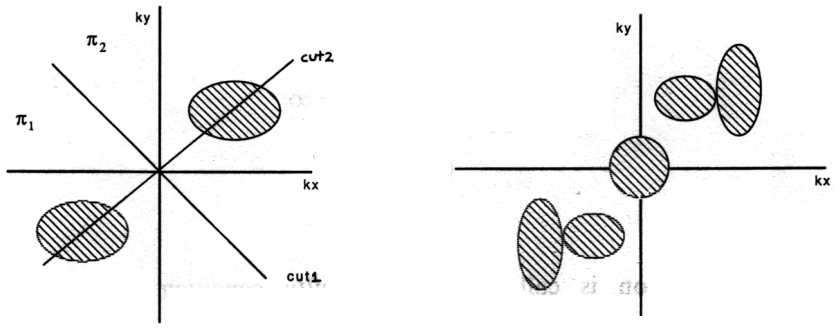

(*a*) (*b*)

Fig. – The partition of **k**-space into π^1 and π^2. (*a*) Appropriate (cut 1) and inappropriate (cut 2) choices. (*b*) Function for which there is no choice of appropriate partition.

This arbitrary choice has nevertheless proven to be quite a useful one, and the definition agrees with a kind of intuitive notion of the phase and amplitude of a real function. Since $\hat{f}(\mathbf{k}) = \hat{f}^*(-\mathbf{k})$, one may assume that there exist two unconnected domains, symmetrically distributed in **k**, where $|\hat{f}|$ is not negligible. Each of these domains is itself sufficient to define f. An appropriate partition of **k**-space into π^1 and π^2 must not intersect either domain, as illustrated schematically in Figs 1 *a* and *b*. A more precise justification for this statement will be given in section 5.

The two domains define two functions F_1 and F_2: $F_1 = F_2^*$ and $\Re F_1 = \Re F_2 = 1/2\, f$. Henceforth we choose to call $2F_1$ *the Hardy function associated with f.*

2.3. The reverse transform

Note that it is possible to reverse the wavelet transform. There is one condition on g for this:

$$C_g = \iint \frac{|\hat{g}(\mathbf{k})|^2}{|\mathbf{k}|^2} d\mathbf{k} < +\infty$$

[*cf.* M 1987, 1989]. For the cylindrical wavelet ($g(\mathbf{k}) = \mathbf{g}(k)$), it is easy to show that:

$$f(\mathbf{r}) = \frac{1}{C_g} \cdot \int_{a=0}^{\infty} \iint f_W(a, \mathbf{b})\, g\left(\frac{\mathbf{r}-\mathbf{b}}{a}\right) \frac{da\, d\mathbf{b}}{a^3}, \tag{14}$$

with $C_g = 2\pi \int_{a=0}^{\infty} |\hat{g}(k)|^2/k\, dk$.

Remark: This result is established for $\mathcal{W}f$ on $\mathcal{H}$, but $\mathcal{W}^{-1}\mathcal{W}f \neq f$. However,

$$\mathcal{W}^{-1}\mathcal{W}f = (1/2)\, \mathcal{W}^{-1}\mathcal{W}F = (1/2)\, F,$$

and $\mathcal{W}$ is the bijection of $\mathcal{H}$ onto $\mathcal{W}(\mathcal{H})$.

3.4. Conditions for the wavelet

In summary, attention will be confined to those wavelets which satisfy the following conditions:

$$\iint |g(\mathbf{r})|^2 \, d\mathbf{r} < +\infty$$

$$C_g < +\infty \tag{17}$$

$$g \in \mathscr{H}$$

The second condition is called the *admissibilty condition* and it requires that $\int g(\mathbf{r})\, d\mathbf{r} = \hat{g}(\mathbf{0}) = 0$ (which is also equivalent to (17), if we suppose that its derivatives are limited).

In practice, g is centred around $(0,0)$, (to be like a window) with an average equal to zero. The condition (17) ensures that the transform of a real function is complex.

4. Examples of useful 2-D wavelets

Morlet2D: The first wavelet is a generalisation in R^2 of the wavelet defined in [G & M, 1984] in R. The result is a directional wavepacket, termed here the *Morlet2D* wavelet:

$$g_\alpha : \mathbf{r} \to e^{i\mathbf{k}_0 \cdot \mathbf{r}} . e - \frac{|\mathbf{r}|^2}{2}$$

with $\mathbf{k}_0$ fixed and $\widehat{(\mathbf{e}_x, \mathbf{k}_0)} = \alpha$ (*Fig.* 2 *and* 3). This wavelet is *directional-specific*, and its Fourier transform selects wave-vectors with both a preferred wavenumber *and* orientation, so,

$$\hat{g}_\alpha(\mathbf{k}) = \exp\left(- \frac{|\mathbf{k} - \mathbf{k}_0|^2}{2} \right).$$

Note that conditions (16) and (17) are not strictly satisfied, but they are *almost* satisfied for large enough $|\mathbf{k}_0|$ ($|\mathbf{k}_0| = 5.5$ as in [G & M, 1984]). As discussed already, the cut between π^1 and π^2 in this case is naturally defined as the line orthogonal to $\mathbf{k}_0$.

Arc and Halo. – It is frequently the case in dealing with real 2-D data, that a single preferred direction for $\mathbf{k}$ is either not known *a priori*, or does not exist, as there are non-negligible contributions from wave-vectors with a number of different orientations. Unless the objective is to specifically single out certain $\mathbf{k}$ orientations, the analysis and interpretation of the transformed data is tedious and difficult. The *Arc* and *Halo* wavelets are deliberate attempts to construct useful wavelet functions without any directional specificity.

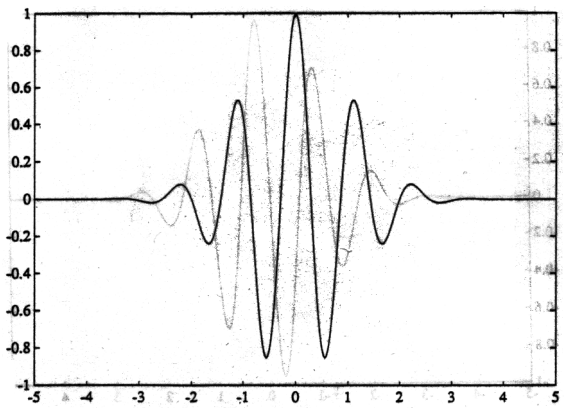

(*a*)

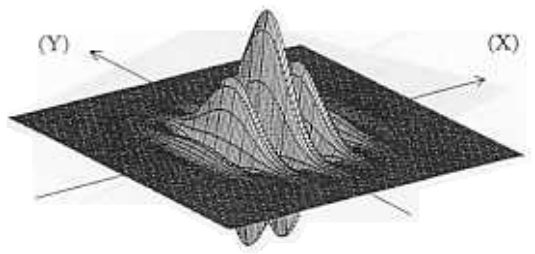

(*b*)

Fig. 2. – Real part of the *Morlet2D* wavelet. (*a*) Cross section at $y=0$ and $\alpha=0$. (*b*) Isometric projection in $[x, y]$.

First, define the real wavelet *Halo*, from (19), but without any direction:

$$\hat{g}_r(\mathbf{k})=\hat{g}_r(k)=\exp\left(-\frac{(|\mathbf{k}|-|\mathbf{k}_0|)^2}{2}\right).$$

As $\hat{g}_r(-\mathbf{k})=\hat{g}_r(\mathbf{k})$, $\hat{g}_r$ is real. With this wavelet, wave-vectors with one well-defined wavenumber are selected, regardless of their direction (compare *Fig.* 4 *a and b*). The attraction of a complex wavelet function, owing to the useful decomposition of the transformed signal into its modulus and argument components has already been pointed out, and so the *Arc* wavelet function is an attempt to combine the lack of directional properties of *Halo* in a basis which remains a Hardy function.

To form the complex wavelet *Arc*, R^2 is partitioned into π^1 and π^2, (3.2 and (12)), where $\hat{g}_c(\mathbf{k})$ is defined as (*Fig.* 4 *c*):

$$\mathbf{k}\in\pi^1; \qquad \hat{g}_c(\mathbf{k})=\hat{g}_r(\mathbf{k}); \qquad \mathbf{k}\in\pi^2; \qquad \hat{g}_c(\mathbf{k})=0$$

The real and imaginary parts of this function are shown in *Figures* 5 *a*, 5 *b* and 6, and clearly the following holds: $\Re\hat{g}_c=(1/2)\,\hat{g}_r$.

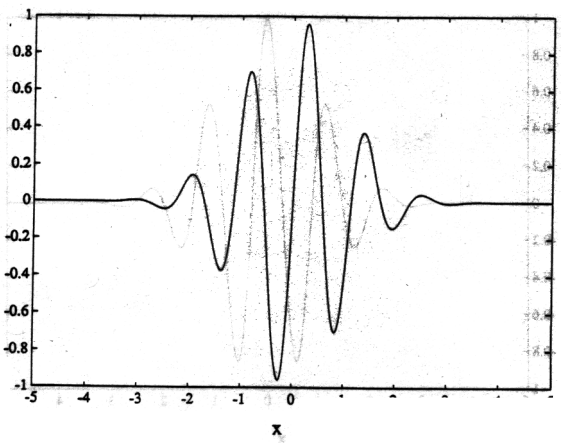

(*a*)

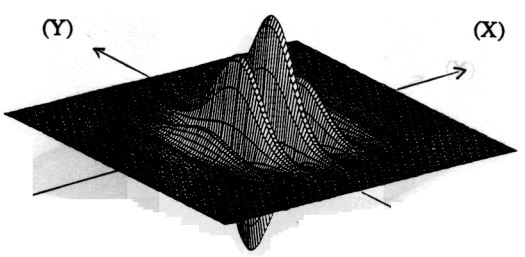

(*b*)

Fig. 3. – Imaginary part of *Morlet2D*. (*a*) Cross section, and (b) Surface view, as in Figure 2.

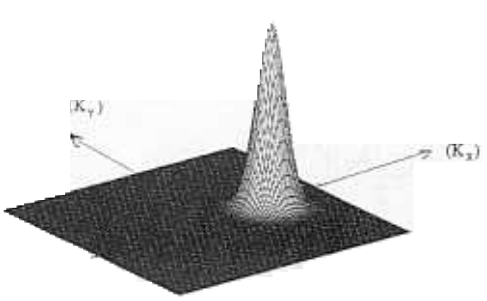

(*a*)

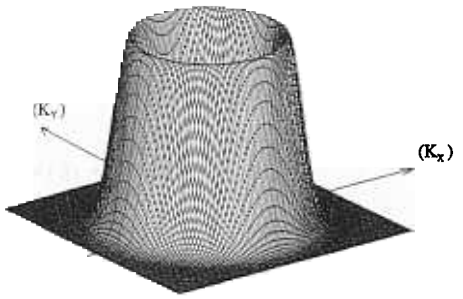

(*b*)

Fig. 4. – The Fourier transforms of 2D wavelets. (*a*) *Morlet2D*, (*b*) *Halo*, and (*c*) *Arc*.

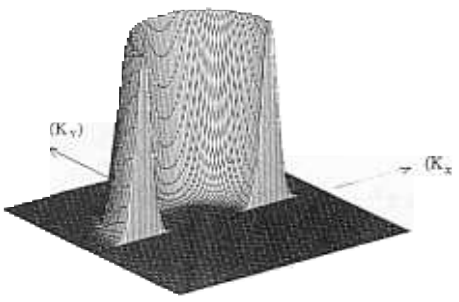

(*c*)

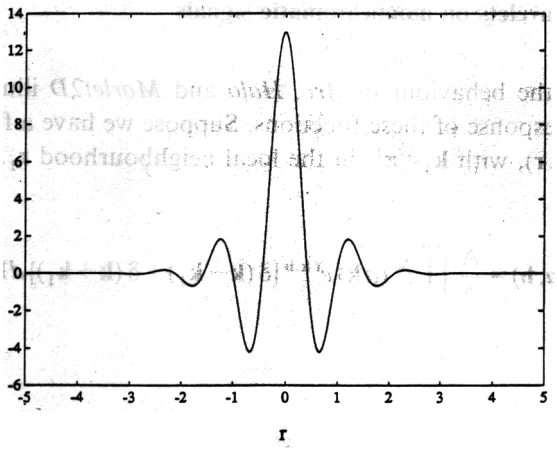

(*a*)

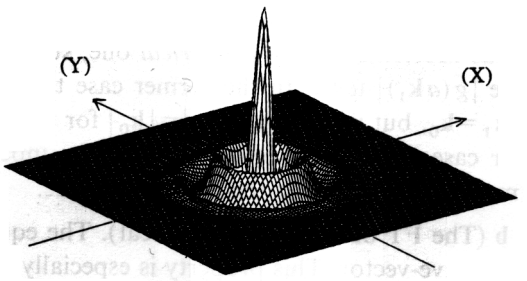

(*b*)

Fig. 5. – Real part of the *Arc* wavelet.
(*a*) Cross section at $y=0$ and $\alpha=0$. (*b*) Isometric projection in $[x, y]$.

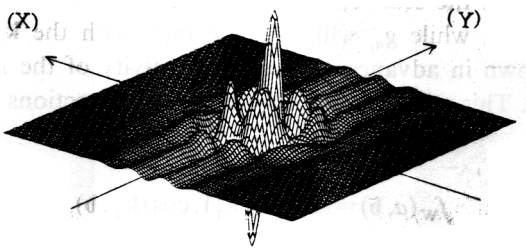

Fig. 6. – Imaginary part of *Arc* in $[x, y]$.

5. Properties of 2-D wavelets on monochromatic signals

A brief analysis of the behaviour of *Arc*, *Halo* and *Morlet2D* illustrates some of the characteristics of the response of these functions. Suppose we have a function, $f(\mathbf{r})$, which behaves like $A\cos(\mathbf{k}_1 . \mathbf{r})$, with $\mathbf{k}_1 \in \pi^1$, in the local neighbourhood $\mathbf{r}_1$. Then its WT for $\mathbf{b}$ around $\mathbf{r}_1$ is,

$$f_W(a, \mathbf{b}) = \frac{A}{2} \iint \hat{g}^*(a\mathbf{k})\, e^{i\mathbf{k}.\mathbf{b}} [\delta(\mathbf{k}-\mathbf{k}_1) + \delta(\mathbf{k}+\mathbf{k}_1)]\, d\mathbf{k}.$$

If $g \in \mathcal{H}$,

$$f_W(a, b) = \frac{A}{2} . \hat{g}^*(a\mathbf{k}_1)\, e^{i\mathbf{k}_1 . \mathbf{b}},$$

and so the following observations may be made:

- $|f_W(a, \mathbf{b})| = A/2 |\hat{g}(a\,\mathbf{k}_1)|$, which is a function of a only. The difference between a *directional* wavelet, such as *Morlet2D*, and a *cylindrical* one, such as *Arc*, may be clearly seen by inspection of the $|\hat{g}(a\mathbf{k}_1)|$ term. In the former case the maximum value of the WT is obtained when $a\mathbf{k}_1 = \mathbf{k}_0$, but whenever $a|\mathbf{k}_1| = |\mathbf{k}_0|$ for the *Arc* wavelet. One need only vary a in the latter case to find the resonance with an input signal, whereas the range of both a and α must be explored for the directional case.

- $\arg(f_W(a, \mathbf{b})) = \mathbf{k}_1 . \mathbf{b}$ (The FT of our wavelets is real). The equiphase lines show the direction of the dominant wave-vector. This property is especially important for the non-directional wavelet like *Arc*, where the phase of the transform, for any resonance value, immediately gives the direction of the wave-vector. The wavenumber can also be verified by looking at two consecutives equiphases separated by 2π.

Once the orientation of the dominant wave-vectors in the data are known, one may deliberately choose to use a direction-specific wavelet (such as *Morlet2D*), at these angles, in order to increase the selectivity and precision of the analysis. This is not so interesting for 'clean' test functions, where the various $\mathbf{k}_i$ are superposed without noise, and the transform of such a function will thus have identical values of both g_c and g_{α_i} at $a_i = k_0/k_i$. However with real experimental data, it may be significant. Consider the behaviour of the cylindrical wavelet at the scale a_i, where it will resonate with all components of the noise at wavenumber k_i, while g_{α_i} will resonate only with the $\mathbf{k}_i$ component. In these cases, where α_i is known in advance, the extra selectivity of the *Morlet2D*-type wavelet may be an advantage. This will be demonstrated on test functions in section 7.

If $g \notin \mathcal{H}$,

$$f_W(a, \mathbf{b}) = A . \hat{g}^*(a\mathbf{k}_1) . \cos(\mathbf{k}_1 . \mathbf{b}).$$

This is the form of the result with *Halo*, or any other real cylindrical wavelet. First, one cannot define a phase for the function. Second, because the transform is a function of both variables a and $\mathbf{b}$, it becomes difficult to distinguish, on the one hand, behaviour

corresponding to spatial changes of scale, a, and on the other hand, the spatial variation of $\cos(\mathbf{k}_1 . \mathbf{b})$ corresponding to the wave-vector at this a, *i.e.* the rôle of $\mathbf{b}$.

It is for this reason that we use only wavelets in $\mathscr{H}$, so as to take full advantage of the fundamental WT property of duality in spectral and physical spaces.

Having introduced the properties of the wavelet function on monochromatic signals, the earlier remarks on the appropriate partitioning of wavenumber space (§ 3.2) may be justified more explicitly. The notion of Hardy space may be retained without difficulty in the extension of the Morlet-type wavelet to its directional equivalent in 2-D, as in *Morlet2D*. For the cylindrical wavelet, one must make a choice in partitioning wavenumber space, defining $\mathscr{H}$ according to the line of partition. Consider the example:

$$f(\mathbf{r}) = \cos[\mathbf{k}_1^+ . \mathbf{r}] + \cos[\mathbf{k}_1^- . \mathbf{r}],$$

with $\mathbf{k}_1^+ = \mathbf{k}_1 + \delta k \mathbf{n}$ and $\mathbf{k}_1^- = \mathbf{k}_1 - \delta k \mathbf{n}$ $(\mathbf{n} . \mathbf{k}_1 = \mathbf{0})$. Suppose $\delta k / k_1 \ll 1$, then the Fourier transform of f is (Fig. 7),

$$\hat{f}(\mathbf{k}) = \frac{1}{2}[\delta(\mathbf{k} - \mathbf{k}_1^+) + \delta(\mathbf{k} + \mathbf{k}_1^+) + \delta(\mathbf{k} - \mathbf{k}_1^-) + \delta(\mathbf{k} + \mathbf{k}_1^-)].$$

The phase of the wavelet transform should specify the direction of $\mathbf{k}_1$, having the form: $\rho e^{(i\,\mathbf{b}.\mathbf{k}_1)}$, $\rho \in \mathbf{R}$. If the wavenumber space is partitioned with the solid line (cut 1) of

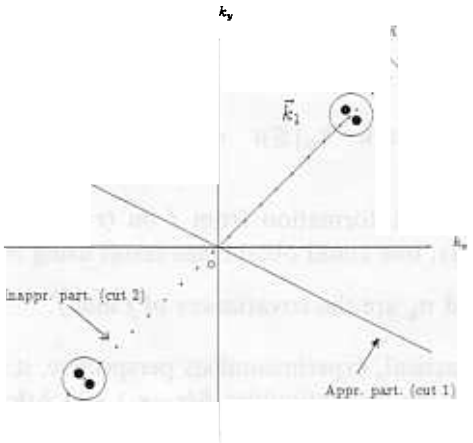

Fig. 7. – The partition of $\mathbf{k}$-space into π^1 and π^2 for a signal with two closely-spaced components in $\mathbf{k}$.

Figure 7, where the intersection is far from the localised wave-vectors, one obtains:

$$f_W(a, \mathbf{b}) = \hat{g}^*(a\mathbf{k}_1) e^{(i\,\mathbf{k}_1 . \mathbf{b})} + \delta k^2 ($$

If, however, a cut is made through the wavenumber domains of interest (cut 2, *Fig.* 7), f_W is,

$$f_W(a, \mathbf{b}) = \hat{g}^*(a\mathbf{k}_1) \cos(\mathbf{k}_1 . \mathbf{b}) + \delta k ($$

The partition of a cylindrical real wavelet (such as *Halo*) to obtain a complex one (such as *Arc*), must be made with care if we wish to retain the correct phase information.

6. Resolution

Let us make some final remarks on the accuracy in physical and Fourier space. Suppose the function $f(\mathbf{r})$ is decomposed on the basis: $(\delta_{\mathbf{r}_1})_{\mathbf{r}_1 \in \mathbf{R}^2} : \mathbf{r} \to \delta(\mathbf{r}-\mathbf{r}_1)$. Here one has maximum possible accuracy in physical space, but no accuracy in Fourier space. On the other hand, with the basis, $(e^{i\mathbf{k}_1 \cdot \mathbf{r}})_{\mathbf{k}_1 \in \mathbf{R}^2}$, the reverse is true. The decomposition on the family of functions generated by a wavelet represents some point in between these two extremes, with finite, but not optimal, accuracy in both spaces with $f_W(a, \mathbf{b})$ being the component on $g_{a,\mathbf{b}}$. Mallat [M, 1989] has effectively used this property in compiling cascades of wavelet transforms, increasing in a, for the 1-D WT multifrequency channel decomposition of images. As a increases, the resolution *decreases* in physical space and *increases* in Fourier space. This is simple to understand by reference to (3) and (4). Consider $g_{a_1,\mathbf{b}_1}$, where a_1 and $\mathbf{k}_1$ are related by $a_1 = |\mathbf{k}_0|/|\mathbf{k}_1|$. Let 2λ be the size of the window around (0,0) defined by g, and let 2μ be the size of the window around $\mathbf{k}_0$ defind by $\hat{g}$. From (3),

$$\left|\frac{\mathbf{r}-\mathbf{b}_1}{a_1}\right| \leqq \lambda \quad \Leftrightarrow \quad |\mathbf{r}-\mathbf{b}_1| \leqq \lambda a_1,$$

and from (4),

$$|a_1\mathbf{k}-\mathbf{k}_0| \leqq \mu \quad \Leftrightarrow \quad |\mathbf{k}-\mathbf{k}_1| \leqq \frac{\mu}{a_1}$$

Then $f_W(a_1, \mathbf{b}_1)$ contains information from f on $(\mathbf{r}=\mathbf{b}_1, \mathbf{k}=\mathbf{k}_1)$ with $|\Delta\mathbf{r}| = a_1\lambda$ and $|\Delta\mathbf{k}| = \mu/a_1$. Alternatively, one could obtain this result using the *uncertainty relation*, $\sigma_{\mathbf{r}} \cdot \sigma_{\mathbf{k}} \leqq \frac{1}{2}$, where $\sigma_{\mathbf{r}}$ and $\sigma_{\mathbf{k}}$ are the covariances of f and $\hat{f}$.

In general, from a practical, experimentalists perspective, it is of interest to know how precisely one can detect the discontinuities $\delta(\mathbf{r}-\mathbf{r}_1)$ and $\delta(\mathbf{k}-\mathbf{k}_1)$ in their own spaces, from their transforms. Both could be present together in experimental data for example as a monochromatic signal with discontinuities (§7.1); consequently, the resolution in both spaces is of concern. As f_W is a function of $(a, \mathbf{b})$, rather than of $(k, \mathbf{b})$, it is preferable to consider the uncertainty in a-space instead of wavenumber space. So (23) may be written as:

$$|ak_1 - k_0| \leqq |a\mathbf{k}_1 - \mathbf{k}_0| \leqq \mu \quad \Rightarrow \quad |a-a_1| \leqq \frac{\mu}{k_1} = \frac{\mu}{k_0}a_1 \quad \Leftrightarrow \quad \Delta a_1 | = \frac{\mu a_1}{k_0}$$

Similarly, from (22), and considering the variable $\mathbf{b}$,

$$|\Delta\mathbf{b}^1| = a_1\lambda.$$

In these variables, both uncertainties increase as a increases (as we shall *see* in section 7.1). Equivalently, the ratios

$$\frac{|\Delta \mathbf{b}_1|}{a} = \lambda \qquad \text{and} \qquad \frac{|\Delta a_1|}{a_1} = \frac{\mu}{k_0}$$

are independent of the scale a.

In the light of these remarks, it is natural to enquire whether the wavelet functions considered here provide the best possible resolution. Consider a small generalisation of the *Morlet2D* wavelet, for which λ and μ may be easily defined:

$$g(\mathbf{r}) = \exp\left(i\mathbf{k}_0 . \mathbf{r} - \frac{|\mathbf{r}|^2}{2\sigma^2} \right), \tag{26}$$

with

$$\hat{g}(\mathbf{k}) = \sigma^2 \exp\left(-\sigma^2 \frac{|\mathbf{k} - \mathbf{k}_0|^2}{2} \right).$$

(For *Morlet2D*, $\sigma = 1$ and $k_0 = 5.5$). $\lambda = \sigma$ and $\mu = 1/\sigma$, so,

$$\frac{|\Delta \mathbf{b}_1|}{a_1} = \sigma \text{ or } (k_1 |\Delta b_1|) = \sigma k_0,$$

$$\frac{|\Delta a_1|}{a_1} = \frac{1}{\quad}$$

Although σ and k_0 might be tuned to adapt to improved signal resolution, $(k_1 |\Delta \mathbf{b}_1|)$ cannot be reduced without limit owing to the conditions (16) and (17),

$$\hat{g}(\mathbf{0}) = \sigma^2 \exp\left(-\frac{\sigma^2 k_0^2}{2} \right) \simeq 0,$$

which, practically speaking, require that $\sigma k_0 > 5$. Even if it were possible to decrease σk_0 and, consequently, $(k_1 |\Delta \mathbf{b}_1|)$, $|\Delta a_1|/a_1$ would be correspondingly increased, as can be seen, either from the relations above, or from consideration of the uncertainty principle.

7. Wavelet transforms of test functions

The performance of each of the wavelet functions on selected test signals illustrates certain of the properties of the function. The test signals have been chosen to emphasize and isolate those characteristics which may be of interest in real applications. The *Arc* wavelet requires that a choice be made for partitioning wavenumber space into π^1 and

π^2, and this choice itself may be made contingent on the distribution of information there, but, for simplicity, in all the *Arc* tests below we define $\pi^1 : y>0$ and $\pi^2 : y<0$.

7.1. Noise-free wave patterns (Carré)

The first test signal (*Fig.* 8) divides $[x, y]$ into four quadrants with two wavenumbers and three orientations.

$$f(x,y)=\cos[\mathbf{k}\,.\,\mathbf{r}]$$

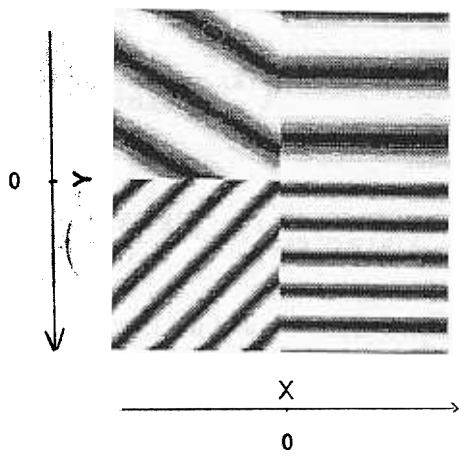

Fig. 8. – Test function Carré. $k_1=0.5$, $k_2=0.2$.

with:

- $\mathbf{k}=k\ (\mathbf{e}_x\cos\beta+\mathbf{e}_y\sin\beta)$
- $k=k_1$ for $y>0$ and $k=k_2$ for $y<0$
- $\beta=\pi/2$ for $x>0$; $\beta=\pi/4$ for $x<0$, $y>0$; $\beta=-\pi/3$ for $x<0$, $y<0$.

Note that β is defined for a coordinate system whose origin is in the top left corner of the test signal. Each quadrant is associated with a different wave-vector $\mathbf{k}$, there is no overlap between the distributions of $\mathbf{k}$, and the signal has no random or coherent noise in it. The interest is to demonstrate the localisation properties of the transform in physical and wavenumber space. *Figures* 9*a* and *b* show the equiphases of the WT of f, using g_c(Arc) for the values of a at the resonances associated with k_1 and k_2. As the Arc wavelet is cylindrical, one immediately has information on both the *direction* of the four wave-vectors and their *domains*. In the space representation of the phase of the transform, the threshold *cut* has been introduced so that the phase is only plotted when,

$$|\mathcal{W}f|>m+(\mathrm{M}-m)\,cut,$$

with,

$$m=\min|\mathcal{W}f(a,.)|,\qquad \mathrm{M}=\max|\mathcal{W}f(a,.)|,\qquad 0\leqq cut\leqq 1$$

The localisation of the modulus of the transform in a and $\mathbf{b}$ ($=y$, with x fixed) are shown in *Figures* 10*a* and *b* respectively. For the points A($x<0$, $y>(0)$ and

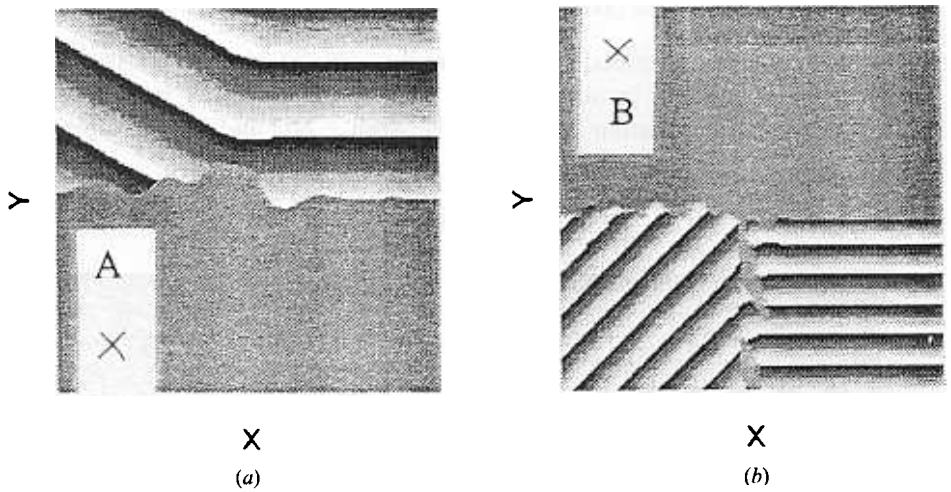

Fig. 9. – Argument of the *Arc* transform of Carré.
(*a*) $a=11$, cut = 60%. (*b*) $a=27$, cut = 60%.

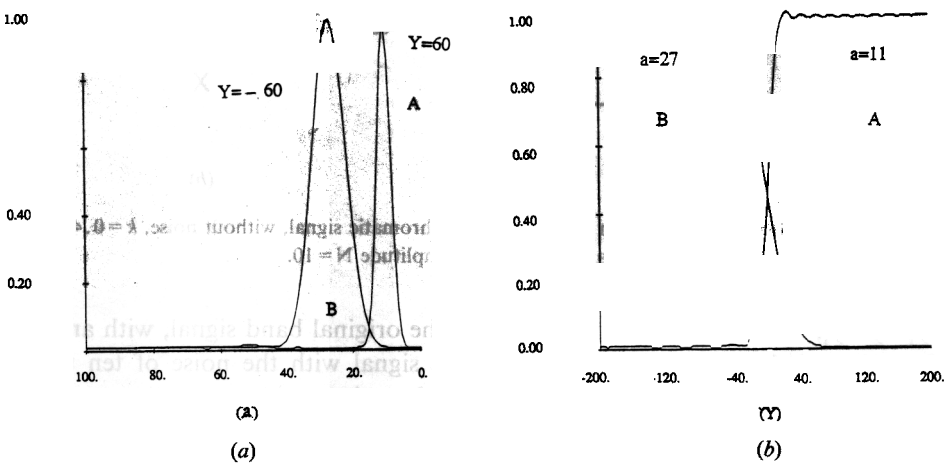

Fig. 10. – Modulus of the *Arc* transform of Carré. (*a*) $|\bullet_{\,f}(a, \mathbf{b})_{\mathbf{b}}|$ at $b_x = x = -60$ and $b_y = y = \pm 60$.
(*b*) $|\bullet_{\,f}(a, \mathbf{b})_{a}|$ at $b_x = -60$, for $a = 11$ and $a = 27$.

B ($x<0$, $y<0$), fixed in different domains, we represent:

$$\mathcal{W}f\,(a, x_{\text{A or B}}, y_{\text{A or B}})\,| = \text{function}_{\text{A or B}}(a)$$

$$\mathcal{W}f\,(a_{\text{A or B}}, x_{\text{A or B}}, y)\,| = \text{function}_{\text{A or B}}(y)$$

and both of these functions have been normalised with M. The first shows how at lower values of a (higher **k**), the localisation in a is improved, as discussed in the previous section. In *Figure* 10*b* the smaller slope at the edge of $|\mathcal{W}f|$ for larger a shows the decrease in resolution in physical space with increasing scale (a).

7.2. Wave patterns with noise (band)

Here, a linear congruential pseudo-random number generator with uniform deviates is used to add high amplitude, incoherent noise to a spatially-limited uniform sinusoid. Noise of amplitude N (the random numbers lie between $-N/2$ and $N/2$) is superimposed on the function:

$$f(x, y) = \cos[\mathbf{k}_1 . \mathbf{r}] \tag{28}$$

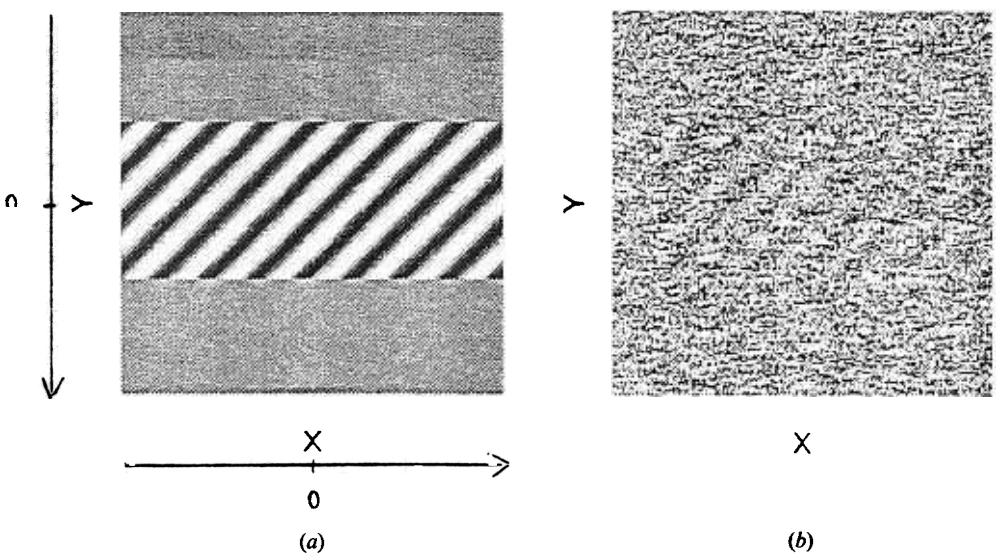

Fig. 11. – Construction of test function Band. (*a*) Monochromatic signal, without noise, $k = 0.4$, $\beta = \pi/4$. (*b*) Signal + noise with amplitude $N = 10$.

for $-y_l < y < y_l$, $x \in \mathbf{R}$. *Figures* 11 *a* and *b* show the original band signal, with an orientation $\beta = \pi/4$, and then the superposition of this signal with the noise of ten times the signal amplitude. How does the Arc wavelet perform in attempts to separate the signal from the noise in both physical and wavenumber space?

Figures 12 *a* and *b* show the equiphase lines of the Arc transform for the resonance at k, first with no threshold, and then with a cut at 0.4 times the amplitude of the modulus of the transform ($|\mathcal{W}f|$). The direction, β, the wavenumber, k, and the band domain are recovered with reasonable accuracy. Since high amplitude noise covers the entire domain, it is less straightforward for a simple threshold cut to delineate the exact border of the band.

In order to form a quick numerical estimate of the relative amplitudes of the transforms of the signal and noise components, the modulus of the transform in transects around (0, 0) was compared for noise alone and for the global signal in *Figures* 13 and 14. These figures also demonstrate the localising properties of the transform in physical and wavenumber space.

First, *Figures* 13 *a* and 14 *a* plot $|\mathcal{W}f(a, x=0, y=y_i)|$, where the y_i are discrete values of y, $-100 < y < 100$, and $|\mathcal{W}$ is normalised by M. The resonance at the small scales

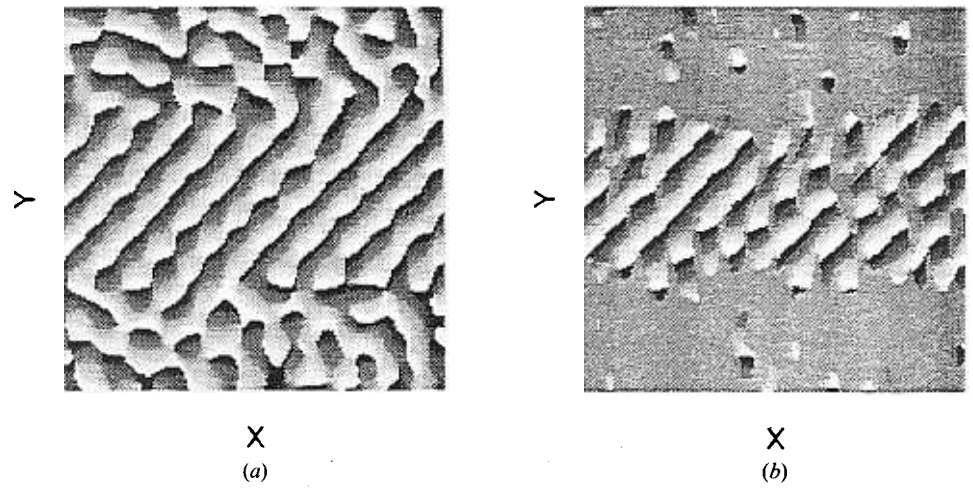

Fig. 12. – Argument of the *Arc* transform of Band.
(*a*) $a=14$, no cut. (*b*) $a=14$, cut = 40%.

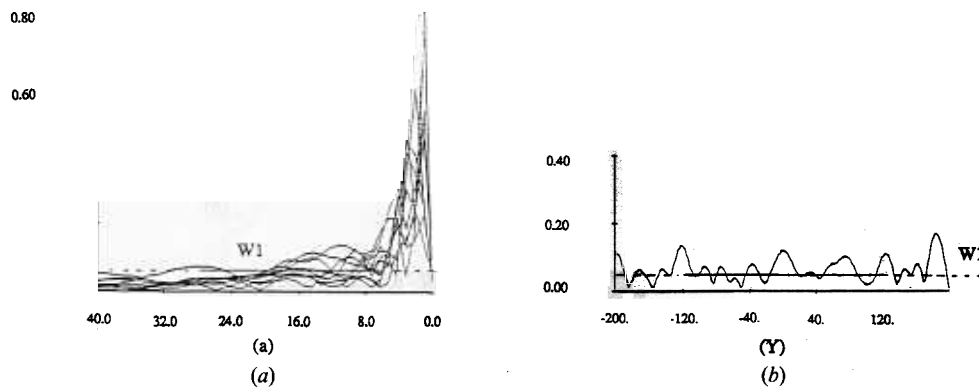

Fig. 13. – Modulus of the *Arc* transform of the noise component of Band.
(*a*) At $x=0$, for a number of transects at $-100<y<100$. (*b*) At $x=0$, $a=14$.

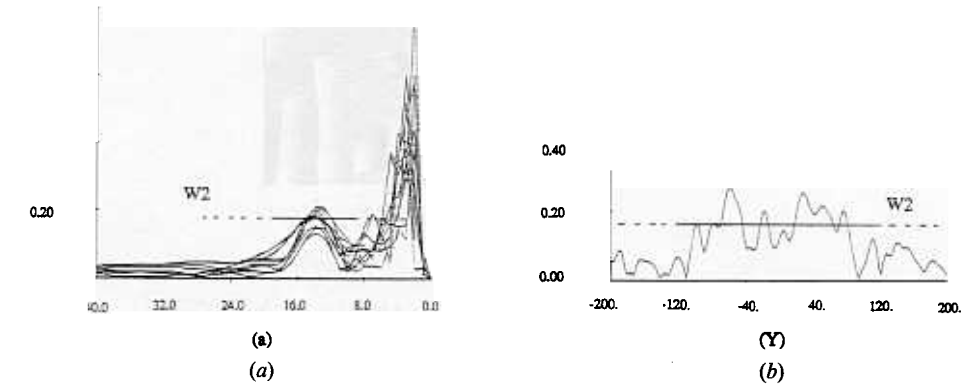

Fig. 14. – Modulus of the *Arc* transform of Band.
(*a*) At $x=0$, for $-100<y<100$. (*b*) At $x=0$, $a=14$.

due to the noise is quite clearly separated from the peak at a_k. Second, *Figures* 13*b* and 14*b* show the localisation of $|\mathcal{W}f(a_k, x=0, y)|$, on the spatial domain Oy. In both cases, one may define the capacity of resolution between noise and the wave at a point by: $|(\mathcal{W}_2-\mathcal{W}_1)/(\mathcal{W}_1+\mathcal{W}_2)|$, where $\mathcal{W}_1$ is the mean value of $|\mathcal{W}f|$ around a (*Fig.* 13*a*) or Oy (*Fig.* 13*b*) for noise alone, and $\mathcal{W}_2$ is the mean value for the signal plus noise (*Fig.* 14). The mean values were 0.47 in physical space and 0.48 in Fourier space with g_c,

This example may be used to compare the cylindrical and directional wavelets of *Arc* and *Morlet2D* (§4). The results discussed thus far in *Figures* 12-14 have been with the cylindrical *Arc* wavelet. Figures 15 and 16 show the *Morlet2D* results, for different

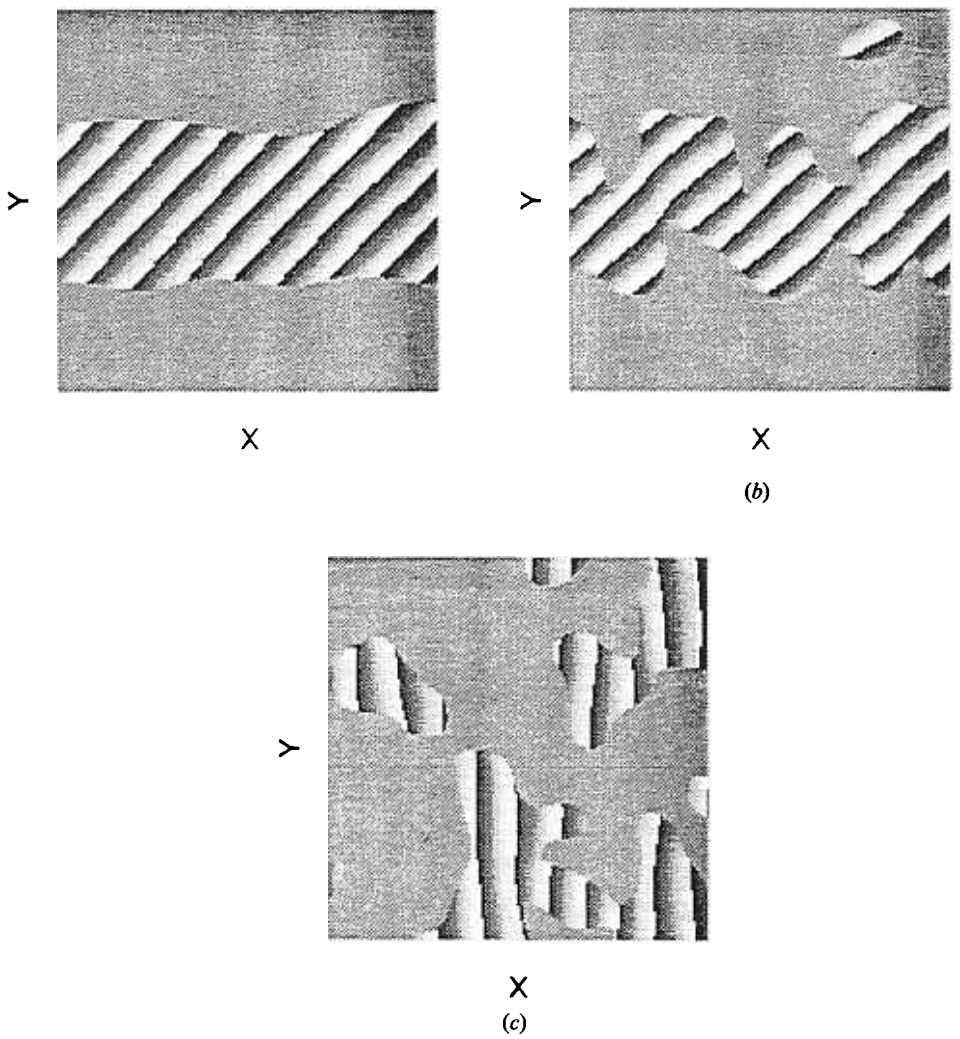

Fig. 15. – Argument of *Morlet2D* transform of Band for $a=14$, cut = 40%.
(*a*) $\alpha=\pi/4$. (*b*) $\alpha=\pi/3$

directions of $\mathbf{k}_0$ at a_k. Compare first of all, *Figure* 15*a* for *Morlet2D*, with *Figure* 12*b* for *Arc*, under the same conditions, and where the wavelet direction exactly corresponds

to the direction of the signal ($\alpha=\beta=\pi/4$). The spatial resolution is significantly improved, and the selectivity is clearly greater. This is hardly surprising since the number of conditions for resonance at a_k have been reduced to only those with the correct orientation. Consequently, as the direction of *Morlet2D* deviates from this angle ($\alpha=\pi/3, 0$), in *Figures* 15*b* and 15*c*, the information from the band itself is lost, as the equiphase lines correspond to the $\mathbf{k}_\alpha$ component of the noise. That the signal to noise ratio of the *Morlet2D* transformed data is superior to that of a non-directional wavelet, such as *Arc*, when the correct direction is known, is apparent also from Figures 16a and *b* (cf.

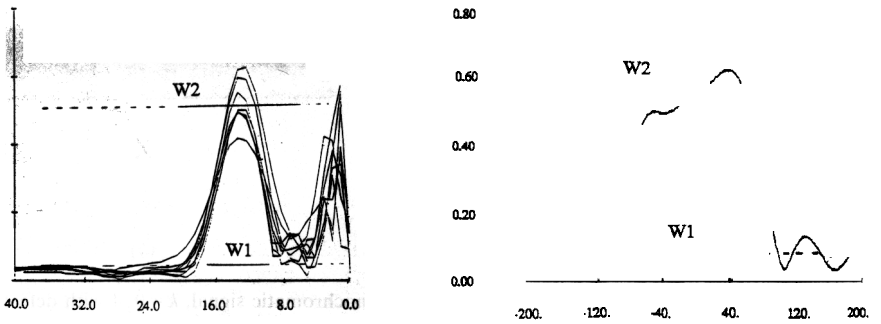

(*a*) (*b*)

Fig. 16. – Modulus of Morlet2D transform on Band ($\alpha=\pi/4$).
(*a*) At $x=0$, for $-100<y<100$. (*b*) At $x=0$, $a=14$.

Fig. 14*a, b*). The capacity of resolution, as defined previously, now may be estimated at 0.85 in physical space, and 0.79 in Fourier space, for $\hat{g_\beta}$. However, unless one has prior knowledge of the direction of the dominant wavevector, this advantage completely disappears.

This suggest the following sequence of steps for the most accurate localisation (in both spaces) of an input signal: first, use *Arc* to determine the domain and directions of the dominant wavevectors, and then, if one wishes to separate them, do so with *Morlet2D* at the appropriate $\mathbf{k}_0$.

7.3. Wave patterns with defects and noise (DEFECT)

The last test function (*Fig.* 17*a*) is a monochromatic signal with a defect [Berry, 1980] at (0, 0):

$$f(x,y)=\frac{\mathrm{F}}{|\mathrm{F}|} \qquad \text{with} \quad \mathrm{F}(x,y)=(x+i\tau y)\,e^{i\mathbf{k}_1\cdot\mathbf{r}}, \tag{29}$$

with $\tau=0.8$, $\beta=\pi/2$ and $k=0.4$. To this function we add two types of noise: the random noise as introduced in Band, and a subharmonic, $-\mathrm{A}(\cos((k/2)y)$, considered as an example of coherent noise, and noise is simply defined as a signal without interest. Qualitatively, one cannot deduce the existence of the signal at all in the composite signal + noise of *Figure* 17*b*, when both noise components have such high amplitudes (N = 10). Although the Fourier transform would allow their separation in wavenumber

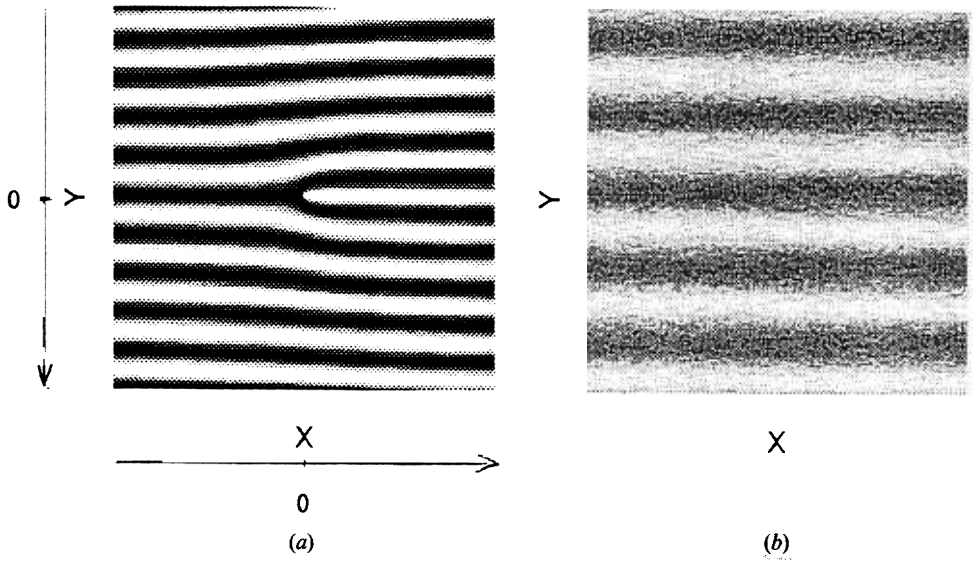

Fig. 17. – Construction of test function Defect. (*a*) Monochromatic signal, $k=0.4$ with defect in (0,0). (*b*) Signal + random noise with amplitude N = 10 and subharmonic with amplitude A = 10.

space, there would be no localisation in physical space, and the existence and location of the defect would be impossible to determine. It is in precisely such instances that one might expect to see the advantages of the wavelet analysis.

Figures 18*a*-18*c* show the argument of the Arc transform on the Defect test signal, for increasing values of a. The first (18*a*) corresponds to $a=8$, which is below any coherent scales in the signal, apart from those generated at random by the first noise component. No regularity is present in the equiphase lines and the modulus of the transform is everywhere small. If $a_k=14$ is chosen exactly at the resonance of the signal, the location of the defect is given very clearly, with only small perturbations in the phase lines due to the noise. Finally, at $a_{k/2}=28$, corresponding to the subharmonic, the wavenumber and orientation of this noise component are isolated.

It is worth re-emphasising that the wavelet transform has enabled the detection, not only of the wavenumber of the camouflaged signal, but also the *defect* and its *exact location*. It is of some interest to be able to directly observe a phase that has an intrinsic definition because such a defect has a phase discontinuity origin. This would be impossible with any real wavelet, such as *Halo*, because there is no phase information, and it would only be possible with a directional wavelet, such as *Morlet2D*, if either the direction information were provided in advance, or an exhaustive search of all possible orientations were conducted. Should this information be available (following a first pass with *Arc*, for example), then *Figure* 19*a*, *b* show that the separation in wavenumber space between the original and the subharmonic, and between both of these and the noise, is slightly superior for *Morlet2D* than *Arc*, but the improvement in the former is slight as the two wavenumbers have the same orientation.

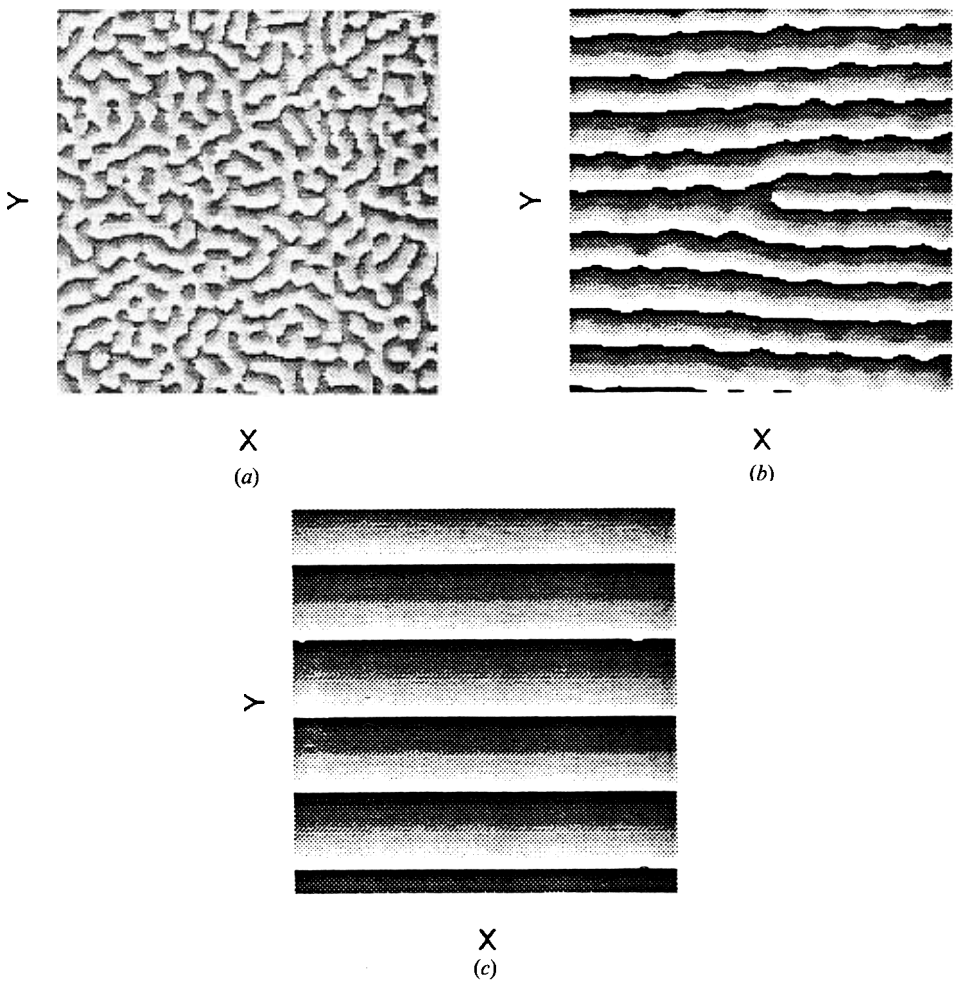

Fig. 18. – Argument of the *Arc* transform of Defect.
(*a*) $a=8$, (*b*) $a=14$, (*c*) $a=28$.

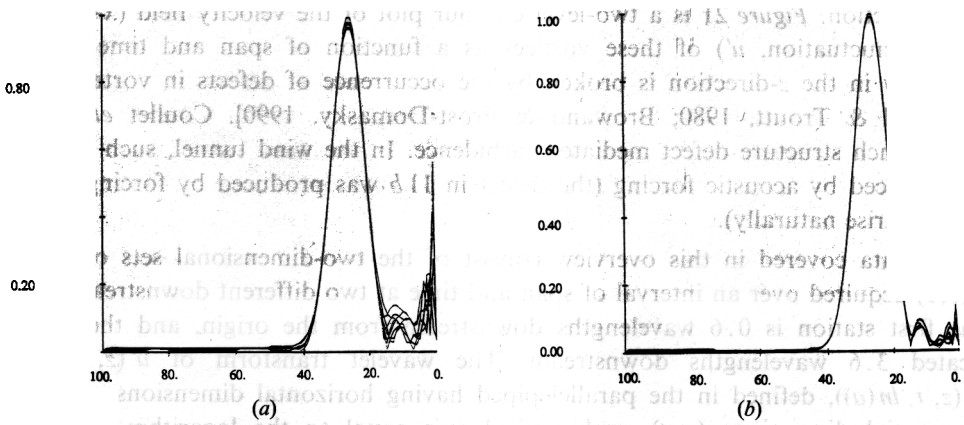

Fig. 19. – Modulus of wavelet transforms of Defect (at $x=0$, $-160<y<160$).
(*a*) *Arc* wavelet. (*b*) *Morlet2D*, with $\alpha=0$.

8. Application to fluid turbulence experiment

An application of the *Arc* wavelet transform to experimental data from a mixing layer demonstrates the new ability to quantify localised scale information that has hitherto been inaccessible *via* conventional means. Here, the lack of directional selectivity of *Arc* is considered a significant advantage in interpretation. In a mixing layer many periods of a wavevector are extended in space and the phase of the *Arc* transform gives useful information concerning the location of defects in the signal.

8 . Scale transitions at defect sites in a mixing layer

In the mixing layer experiment, two unidirectional, parallel streams are separated by a thin plate, terminated as in *Figure* 20. The intensely turbulent region, which forms

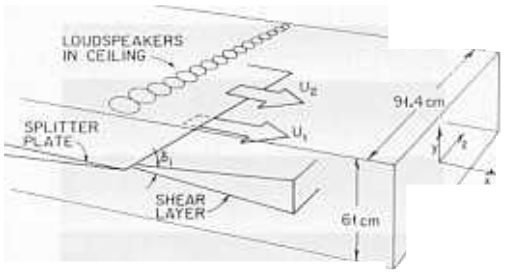

Fig. 20. – Sketch of the mixing layer experiment.

downstream from the plate termination, serves as a (somewhat) idealised model for a variety of shear flows occuring in nature and in technological applications. The important feature of these flows is that the homogeneous dimension in the z-direction is usually several orders of magnitude greater than the vorticity thickness (y-dimension of the boundary layers). Such flows are inherently unstable – the vorticity within the original boundary layers is first reorganized into concentrations of vorticity aligned roughly in the z-direction. *Figure* 21 is a two-level contour plot of the velocity field (x-component velocity fluctuation, u') of these vortices as a function of span and time. However, symmetry in the z-direction is broken by the occurrence of defects in vortex structure [Browand & Troutt, 1980; Browand & Prost-Domasky, 1990]. Coullet *et al.* [1989], termed such structure defect mediated turbulence. In the wind tunnel, such defects can be produced by acoustic forcing (the defect in 11 *b* was produced by forcing, although they do arise naturally).

The data covered in this overview consist of the two-dimensional sets of values of $u'(z, t)$ acquired over an interval of span and time at two different downstream stations. The first station is 0.6 wavelengths downstream from the origin, and the second is located 3.6 wavelengths downstream. The wavelet transform of $u'(z, t)$ will be $f_W(z, t, ln(a))$, defined in the parallelepiped having horizontal dimensions representing the spatial dimensions (z, t), and vertical axis equal to the logarithm of the scale variable a.

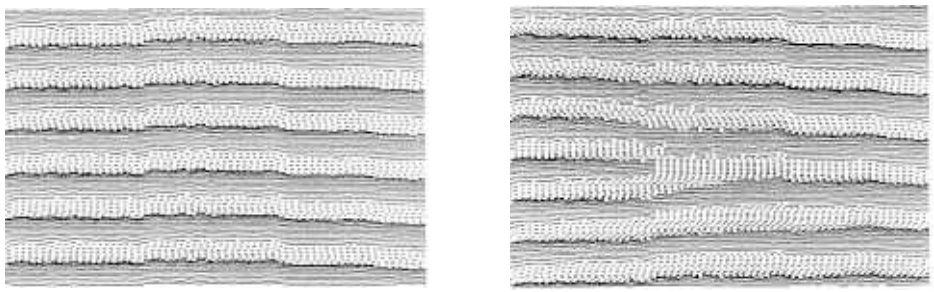

(*a*) (*b*)

Fig. 21. – Contour plot of u' at the measured downstream positions: (*a*) without defect, and (*b*) with defect.

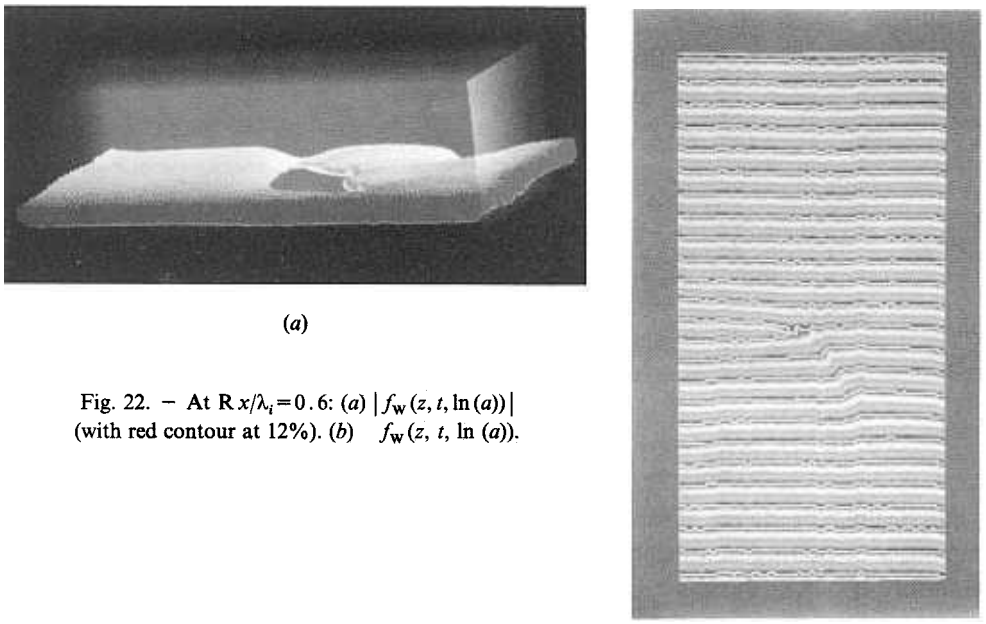

(*a*) (*b*)

Fig. 22. – At R $x/\lambda_i = 0.6$: (*a*) $|f_W(z, t, \ln(a))|$ (with red contour at 12%). (*b*) $f_W(z, t, \ln(a))$.

Figure 22 *a* shows $|f_W|$ at the first downstream station. The contour described in red represents 12% of $|f_W|_{max}$ at the first station. The prominent red band defines a particular scale a (or wave length, $\lambda = 1.143\,a$) which dominates the scene. There is, however, a hole in the band near the center of the domain, and this represents a diminished amplitude in the vicinity of the defect. The defect can be clearly seen in the 2-D phase portrait at the value of a in the centre of this band (*Fig.* 22 *b*). At the farther downstream station, an interesting evolution is evident in *Figure* 23 *a*. The defect is the site of an explosive growth of larger scales. The process of scale growth is centered at a scale which is a factor of two greater than the initial scale (as the additional contour in *Figure* 23 *b* shows, at 61% of the $|f_W|_{max}$ at the first station), but there is a large bandwidth about this

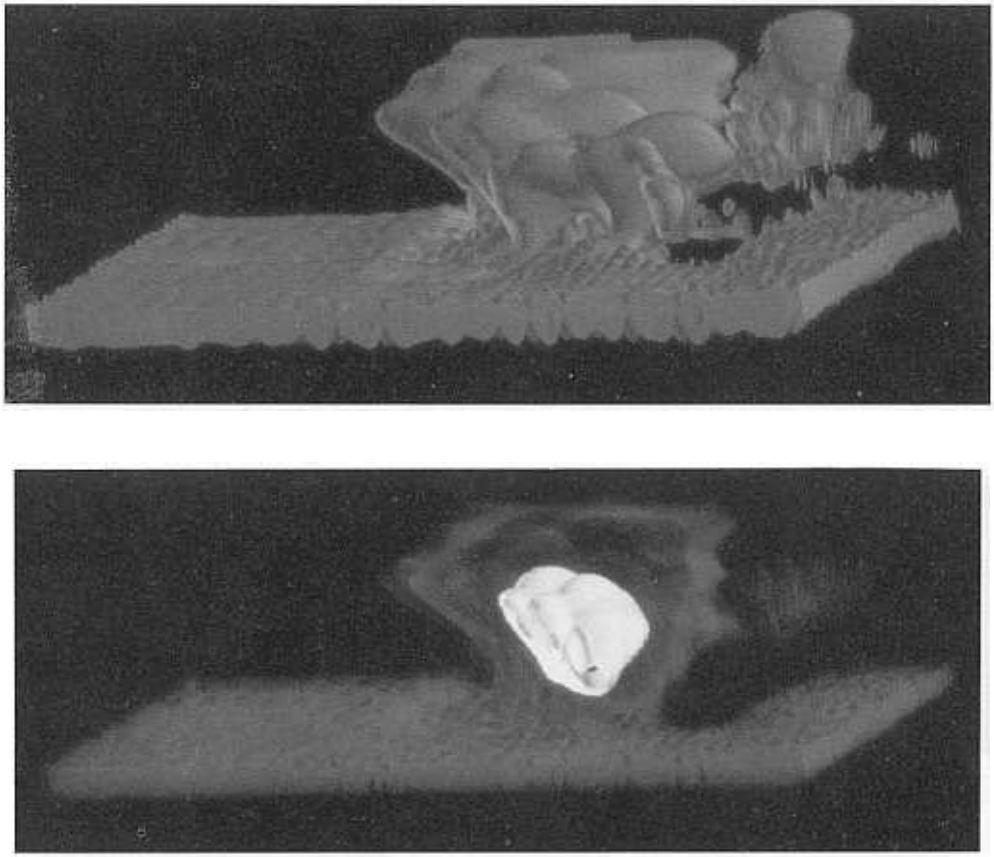

(*b*)

Fig. 23. - $|f_w(z, t, \ln(a))|$ at $Rx/\lambda_i = 1.8$, with no forcing of the subharmonic: (*a*) Red contour at 12%. (*b*) White contour at 61%.

value. Physically, the defect seems to act as the seed which promotes a local vortex amalgamation or pairing of vortices. A process which was originally presumed to occur nearly uniformly across the span [C *et al.* 1989] is seen here to take on a distinctly three dimensional character.

Forcing the flow in a slightly different format emphasises the local scale transition. The acoustic disturbances which are amplified by the shear layer are very small-on the order of 10^{-4} of a typical flow velocity. If now the subharmonic is locally forced by modulating the width of the acoustic pulses, the response shown in *Figure* 24 *a* obtains at the same downstream station. The region of large scale growth extends over a broader region of space. The interior contour in *Figure* 24 *b* also suggests that growth is centered more narrowly about the scale 2 λ.

Finally, a more global forcing of the subharmonic deemphasises the local aspect of the scale transition (*Fig.* 25), which now takes place rather uniformly over the entire plane. There is a region of diminished amplitude at scale corresponding to 2λ slightly downstream of the original defect. The lowered amplitude signifies the beginnings of a new defect region, as can be seen from the phase contours in *Figure* 25 *b*. Of course, the

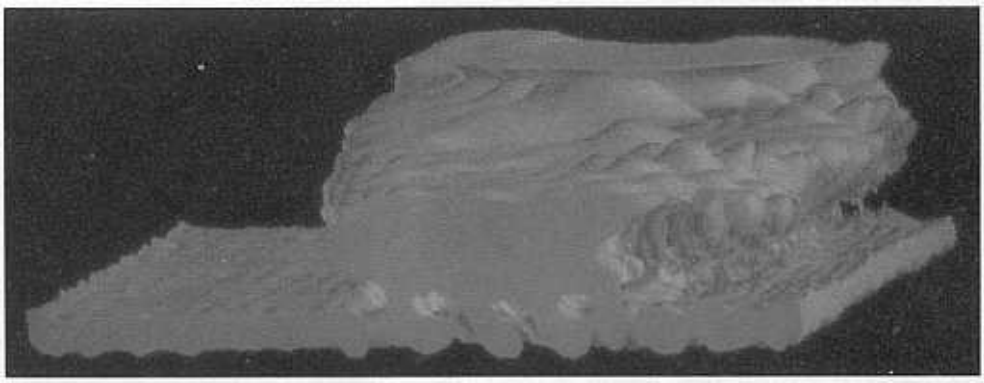

(*a*)

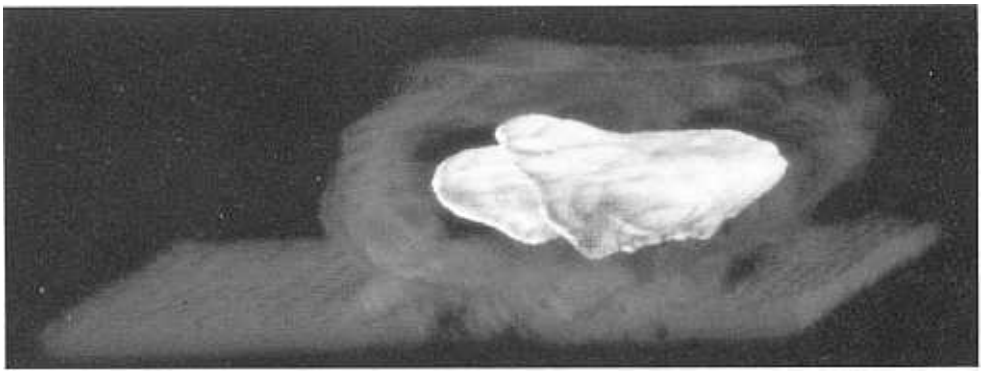

(*b*)

Fig. 24. - $|f_W(z, t, \ln(a))|$ at R $x/\lambda_i = 1.8$, with local forcing of the subharmonic. (*a*) Red contour at 12%. (*b*) White contour at 61%.

analysis can be made in a quantitative fashion, and localised measures of the energy density allow the relative effects to be measured in detail. A comprehensive quantitative analysis appears in Dallard & Browand [1992].

This evidence illustrates the delicate balance between local defect-induced transition, and global transition. Either situation can be promoted by small amounts of appropriate forcing. There are many problems which require the thorough mixing of two fluid streams, and more efficient mixing might well result from a proper combination of the types of forcings discussed here.

9. Conclusions

The investigation and derivation of new 2-D wavelet functions, and their relationship to those already discussed in the literature has been described. Presently, the most

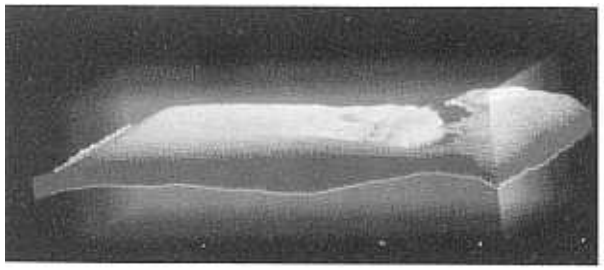

(*a*)

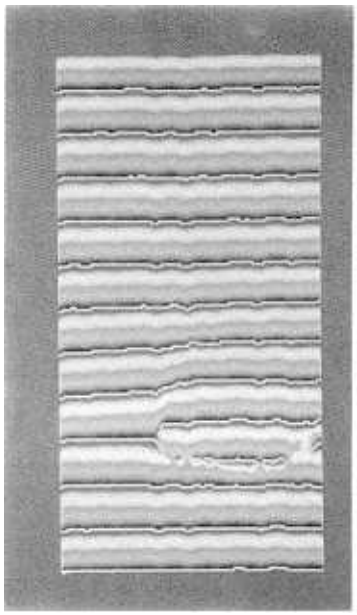

(*b*)

Fig. 25. – At $R\,x/\lambda_t = 1.8$, with global forcing of the subharmonic: (*a*) $|f_w(z, t, \ln(a))|$ (Red contour at 12%). (*b*) $f_w(z, t, \ln(a))$.

generally useful of these wavelets is *Arc*, which has the following desirable characteristics:

- the wavelet is *complex*, and therefore carries information on both the phase and amplitude of the input signal.
- it is *cylindrical*, and thus has no directional selectivity; any wavevectors with $\mathbf{k}_0$ will thus be detected in a signal, regardless of orientation.

These properties have been discussed analytically, and their behaviour has been demonstrated on test functions involving spatially separated wavevectors with different orientation and wavenumber (Carré), spatially-limited monochromatic signals with specific orientation in the presence of high amplitude, incoherent noise (Band), and monochromatic signals with phase discontinuities in the presence of high amplitude coherent and incoherent noise (Defect). This latter case seems especially relevant to the many cases where defects play a significant rôle in the system dynamics. Convection rolls in Rayleigh-Bénard flows, and instabilities in two dimensional mixing layers are two cases in point from the field of fluid dynamics. An example application involving this latter flow shows how the wavelet analysis enabled the contribution of a physically localised phenomenon (phase defects) in 3-D scale transitions to be identified. Both of the characteristics of *Arc* listed above as desirable were in fact essential for this analysis.

It is quite likely that the dual Fourier and physical space localisation properties of the 2-D wavelet transform may play a fundamental role in fluid turbulence investigations [F *et al.*, 1989; L & B, 1990], where the relationship between spectral theories and physical phenomena has never been completely clear. Just as the Fourier transform has acted as a common language between theory and experiment, the wavelet analysis provides a common basis for comparison, but now more easy to interpret in physical space. Indeed, it has been argued [L & B, 1990] that the compact wavelet basis provides a more natural

decomposition of a turbulent fluid flow, corresponding to the dynamics of coherent, localised vortex structures.

Acknowledgements

It is a pleasure to thank Prof. F. K. Browand for invaluable advice and comments on this paper, and throughout the work. The data visualisation and graphics were greatly facilitated by extensive use of the public domain NCSA visualisation software; the translation to grey-scale poscript was due to L. Guez. The financial support of the Office of Naval Research (ONR N00014-86-K-0679) is gratefully acknowledged.

REFERENCES

ANTOINE J. P., CARETTE P., MURENZI R. & PIETTE B., 1992, Image analysis with 2-D continuous wavelet transform: detection of position, orientation and visual contrast of simple objects, *I.E.E.E. Trans. Inf. Theor.*, in press.

ARGOUL F., ARNEODO A., ELEZGARAY J., GRASSEAU G. & MURENZI R., 1988, Wavelet transform of two-dimensional fractal aggregates, *Phys. Rev. Lett. A*, **135**, 327-336.

ARGOUL F., ARNEODO A., ELEZGARAY J., GRASSEAU G. & MURENZI R., 1988, Wavelet analysis of the self-similarity of diffusion-limited aggregates and electrodeposition clusters, *Phys. Rev. A*, **41**, 5537-5560.

ARNEODO A., GRASSEAU G. & HOLSCHNEIDER M., 1988, Wavelet transform of multifractals, *Phys. Rev. Lett. A*, **61**, 2281-2284.

BERRY M., 1980, Singularities in waves and rays, In *Les Houches-Physics of Defects*, 453-541.

BROWAND F. K. & TROUTT T. R., 1980, A note on spanwise structure in the two-dimensional mixing layer, *J. Fluid Mech.*, **917**, 771-781.

COULLET P., GIL L. & LEGA J., 1989, A form of turbulence associated with defects, *Physica D*, **37**, 91-103.

DALLARD T. & BROWAND F. K., 1992, Scale transitions at defect sites in the mixing layer: application of the 2-D *Arc* wavelet transform, *J. Fluid Mech.*, in press.

DAUBECHIES I., 1988, Orthogonal bases of compactly-supported wavelets, *Comm. Pure. Appl. Math.*, **41**, 909-996.

DAUBECHIES I., 1992, *Ten Lectures on Wavelets*, S.I.A.M., Philadelphia.

DAUGMAN J. G., 1988, Relaxation neural network for non-orthogonal image transforms, *Proc. I.J.C.N.N.*, **1**, 547-560.

FARGE M., 1992, Wavelet transforms and their applications to fluid turbulence, *Ann. Rev. Fluid Mech.*, **24**, 395-457.

FARGE M., HOLSCHNEIDER M. & COLONNA J. F., 1989, Wavelet Analysis of Coherent Structures in 2-D Turbulent Flows, In *Topological Fluid Mechanics*, K. MOFFATT Ed., pp. 765-776, Cambridge University Press.

GABOR D., 1945, Theory of Communication, *J. Ins. Electr. Eng.*, **93**, 429-457.

GROSSMAN A. & MORLET J., 1984, Decomposition of Hardy functions into square integrable wavelets of constant shape, *S.I.A.M. J. Math. Anal.*, **15**, 723-736.

GROSSMAN A., COMBES J. M. & TCHAMITCHIAN Ph., 1987, *Wavelets: Time-Frequency Methods and Phase Space*, Springer.

JAFFARD S. & MEYER Y., 1988, Bases d'ondelettes dans des ouverts de R^n, *J. Math. Pures Appl.*, **68**, 95-108.

LARSONNEUR J. L. & MORLET J., 1987, Wavelets and seismic interpretation, In *Wavelets: Time-Frequency Methods and Phase Space*, 126-131, Springer.

LIANDRAT J. & MORET-BAILLY F., 1990, The wavelet transform: some applications to fluid dynamics and turbulence, *Eur. J. Mech. B*, **9** (1), 1-19.

MALLAT S. G., 1989 *a*, Multifrequency channel decompositions of images and wavelet models, *I.E.E.E. Trans. Acoust. Spch. Sig. Proc.*, **37**, 2091-2110.

MALLAT S. G., 1989 *b*, A theory for multiresolution signal decomposition: the wavelet representation. *I.E.E.E. Trans. Patt. Anal. Mach. Intell.*, **11**, 674-693.

MEYER Y., 1987, Orthogonal bases of wavelets with finite support-connection with discrete filters, In *Wavelets: Time-Frequency Methods and Phase Space*, 27-37, Springer.

MEYER Y., 1990, Ondelettes et Opérateurs, *I. Ondelettes. II. Opérateurs de Calderón-Zygmund. III. Opérateurs Multilinéaires*, Hermann, Paris.

MURENZI R., 1987, Wavelet transforms associated to the *n*-dimensional Euclidean group with dilations: signal in more than one dimension, In *Wavelets: Time-Frequency Methods and Phase Space*, 239-252, Springer.

MURENZI R., 1989, *Wavelet Transforms Associated to the n-Dimensional Euclidean Group with Dilations*, Ph. D. Thesis, U.C.L., Louvain-la-Neuve.

TUTEUR F. B., Wavelet transformations in signal detection, In *Wavelets: Time-Frequency Methods and Phase Space*, 132-138, Springer.

(Manuscript received September 17, 1991;
in revised form June 10, 1992;
accepted July 4, 1992.)